

Synthesis of Pt-Ni/CNT Cathodic Catalyst and its Application in a PEM fuel Cell

D. M. López-Rosas¹, R. M. Félix-Navarro², J. R. Flores-Hernández³, C. Silva-Carrillo², I. L. Albarán-Sánchez³, E.A. Reynoso-Soto^{1, 2*}

¹Tecnológico Nacional de México – Instituto Tecnológico de Tijuana. Posgrado en Ciencias de la Ingeniería. C. P., 1166. Tijuana, B. C. 22000, México.

²Tecnológico Nacional de México - Instituto Tecnológico de Tijuana. Centro de Graduados e Investigación. C. P. 1166. Tijuana, B. C. 22000, México.

³Instituto Nacional de Electricidad y Energías Limpias, Ave. Reforma 113 Col. Palmira, Cuernavaca, Morelos, 62490, México.

***Corresponding author:** E.A. Reynoso-Soto, email: edgar.reynoso@tectijuana.edu.mx

Received July 16th, 2020; Accepted November 2nd, 2020.

DOI: <http://dx.doi.org/10.29356/jmcs.v65i1.1268>

Abstract. This work reports the synthesis, characterization, and catalytic activity of Pt-Ni/CNT with a low platinum load to use as cathode electrocatalyst in PEMFC (proton-exchange membrane fuel cells). The synthesis of nickel particles on the carbon nanotubes surface was carried out by chemical reduction of a Ni(ethylenediamine) complex; after that, the galvanic displacement reaction was performed to platinum deposition onto Ni/CNT. The Pt-Ni/CNT was deposited by spray technique on a gas diffuser layer (GDL) and subsequently subjected to several potential cycles to promote Ni atoms migration. Finally, its catalytic activity was evaluated in a fuel cell.

Keywords: Pt-Ni; PEMFC; potential cycles.

Resumen. En este trabajo, se reporta la síntesis, caracterización y evaluación catalítica del electrocatalizador Pt-Ni/CNT con bajo contenido de platino, empleado como electrocatalizador catódico en una celda de combustible tipo PEMFC (Celda de combustible de membrana de intercambio protónico). La síntesis de las partículas de níquel sobre la superficie de los nanotubos de carbono se llevó a cabo mediante la reducción química del complejo de Ni(etylendiamina) y posteriormente, se depositó platino sobre el material Ni/CNT mediante la reacción de desplazamiento galvánico. Se depositó una película de Pt-Ni/CNT sobre un difusor de gas mediante la técnica de esprayado y posteriormente fue sometido a diversos ciclos de potencial para promover la migración de los átomos de níquel y evaluar su actividad catalítica en una celda de combustible.

Palabras clave: Pt-Ni; PEMFC; ciclos de potencial.

Introduction

Nowadays, energy resources have begun to run out, which has generated an increased urgency to look for alternative fuels that are clean and renewable. A viable alternative for clean energy production is using the PEMFC. The PEMFC has attracted much more attention due to their high efficiency, high-power density, easy scale-up, and the lowest operating temperatures [1]. However, Pt catalysts' high cost stimulates interest in developing free or low-content platinum group metal catalysts to replace in PEMFC [2]. Diverse groups have conducted several investigations to enhance Pt catalysts' performance toward oxygen reduction reaction (ORR) in the cathode electrode, including its activity and durability in recent years [3,4]. One alternative to improve cathodic catalysts catalytic activity is supporting the Pt active phase over conductive materials; some of these materials employed are carbon nano-forms like; Vulcan carbon (C) [5], carbon black (NCB) [6], graphenes (GNPs) [7], multi-walled carbon nanotubes (CNT) [8], graphenes with intercalated carbon nanotube [9], graphenes with carbon black [10], and others. Pt electrocatalyst supported on multi-walled carbon nanotubes has diverse advantages compared with other carbon nano-forms for PEMFCs, generating excellent corrosion performance and higher stability in the ORR [11,12]. Further, other alternatives are employed using less Pt and maintaining excellent electrocatalytic performance incorporating a second metal. Numerous studies indicate that Pt and another metal's catalytic activity can enhance ORR [13,14]. Some examples of these bimetallic electrocatalysts are PtM_3/C ($\text{M}=\text{Fe, Co, and Ni}$) [14], PtM/GNPs ($\text{M}=\text{Ni, Fe, and Cu}$) [7], $\text{Pt}_3\text{M}/\text{NCB}$ ($\text{M}=\text{Pd, Fe, and Ni}$) [6], among others.

The cathodic Pt-bimetallic catalyst catalytic activity improvement is due to the changes in electronic properties, composition, structure, particle size, bond, and inter-particle distance. Various studies have proven the formation of Pt-layer over Pt_xM_y catalyst's surface. Pt_xM_y alloys with transition metals change the Pt surface energy, improving the catalytic activity in the ORR, promoting better O_2 adsorption, and reducing the kinetics by a decrease in the Pt-Pt bond distance and a change of electronic structure by the increase of d-electron vacancies of Pt atom by the second metal content [15]. Gan et al. prepared $\text{Pt}_x\text{Ni}_{1-x}$, alloy catalysts and observed an increase in catalytic activity after the dissolution of Ni atoms by electrochemical potential cycles, by the increase in the Hupd area (an increase of electrochemically active area, ECSA) with the dissolution of the 50% of Ni atomic ratio of the catalyst composition, indicating the formation of Pt-layer in a catalyst surface [16]. Becknell et al. have prepared PtNi nanoframes. They observed an effect of Pt/Ni ratios over the ECSAs measured by CO stripping and H adsorption/desorption process, determining high catalytic activity in the ORR with 1.5 ratio and a decrease with 1.0 and fewer ratios [17].

Bimetallic catalyst based on Pt for the ORR has been prepared by diverse methods such as direct chemical reduction, electrodeposition, solvothermal, polyol, ligand coating, and galvanic displacement. These bimetallic catalysts for the ORR have been developed as alloys, dispersions, and core-shell particles. Core-shell catalysts are excellent in the ORR and generally are composed of non-noble transition metal as core and an active noble transition metal as the shell. The core physicochemical characteristic is critical for the distribution of noble metal atoms in the shell surface. The use of stabilizing agents or ligand may influence core-shell nanostructures growth, stability, and surface chemistry because the ligands play multiple roles in the synthesis of these type of particles, like improving the solubility of metallic precursors, as a diffusion barrier, change in the nucleophilicity of metal, stabilizing agent for Ostwald ripening or agglomeration, and as growth director [18]. Galvanic displacement is one of the most effective methods to prepare core-shell particles. The process combines aspects of corrosion and electrodeposition when the less noble metal with a specific physicochemical characteristic interacts with the noble metal ions; these will be reduced due to the difference in the metals redox potential depositing in the surface of non-noble transition metal [19].

Many authors report the synthesis of particles with core-shell structure by galvanic displacement as Pt bimetallic catalyst for the ORR and propose different strategies to improve the catalytic activity like the dealloying and leaching of less noble metal, by thermal treatment, chemical dissolution, or electrochemical process [20-22]. The dealloying and leaching of a core-shell structure can produce a porous structure or frameworks, and different composition of the catalyst and these changes can improve the catalytic activity and stability [23,24].

The size and composition of the core are essential in the synthesis of the core-shell structure. Ethylenediamine (EDA or en) is a bidentate ligand that can be coordinated to metallic ions and metals and leads

to a five-membered complex with many of the cyclopentane stereochemical characteristics. A transition-metal generally shows a high affinity to EDA in comparison with alkaline and alkaline earth metals [25,26]. EDA has been employed to synthesize non-noble metallic and oxide particles in solution or deposited on carbon structures. Yan et al. observed that the variation of EDA concentration presents an effect in the nickel particle size supported on carbon; they report a decrease in the particle size with a high concentration of EDA and aggregation of the particles in the absence of EDA [27]. Zhang et al. reported the synthesis of nickel oxide particles over carbon nanofibers with EDA and propose that the particle size is controlled by forming a hydrogen bond between one amino group of EDA and the surface functional groups carbon nanofibers. In contrast, the nickel ions interact with the other amino group of EDA [28]. The improvement in the synthesis of non-noble metallic or oxide particles, like nickel, in the absence of specific reduction agents or expensive synthetic procedure, is due to the organometallic complex's formation. The addition of N donor ligands, such as EDA, leads to the sequential replacement of the coordinated water molecules and the formation of complexes in mono, bis, and tris ligated forms of the general form $[\text{Ni}(\text{en})_n]^{2+}$ ($n = 1-3$), this complex being very stable even in the presence of very polar solvents controlling the diffusion of growth species. Nickel, in solution in the absence of ligands, tends to interact strongly with the medium; for example, in aqueous systems, it tends to form the $[\text{Ni}(\text{H}_2\text{O})_6]^{2+}$ complex, making hard the reduction because potential redox increase, solubility, and pH values change [29,30].

In this paper, we report the synthesis of the Pt-Ni/CNT cathodic electrocatalyst using EDA. The Pt-layer surface formation was evaluated by CO stripping and H_{upd} for the Pt-Ni/CNT material. The synthesized Pt-Ni/CNT cathodic electrocatalyst with low Pt content and improved performance at applied different activation cycles were applied in PEMFC.

Experimental

Chemicals

Potassium hexachloroplatinate (IV) (K_2PtCl_6 , 98%), nickel chloride hexahydrate (II) (NiCl_2 , 99%), ethylenediamine ($\text{C}_2\text{H}_8\text{N}_2$, 99%), sodium borohydride (NaBH_4 , 99%), Nafion®-117 solution (5%), toluene (C_7H_8 , 99%) and ferrocene ($\text{Fe}(\text{C}_5\text{H}_5)_2$, 98%) were acquired from Sigma-Aldrich®. Methanol (CH_3OH , 99.9%), nitric acid (HNO_3 , 70%), and sulfuric acid (H_2SO_4 , 97%) from Fermont. Nitrogen (N_2 , 99%), oxygen (O_2 , 99%), carbon monoxide (CO , 99%), and argon (Ar , 99 %) gases were purchased from Infra. Aqueous solutions were prepared in Milli-Q water ($18 \text{ M}\Omega$, Thermo scientific).

Synthesis and activation of CNT

CNT_{syn} were prepared by the pyrolysis method. An argon/toluene/ferrocene mixture was fed into the quartz tubing after the tubular oven temperature was set at 850 °C for 30 min at 0.2 mol L⁻¹. CNT_{syn} were dispersed in an aqueous dissolution of the $\text{H}_2\text{SO}_4/\text{HNO}_3$ (1:3 molar ratio) mixture. Then, 200 mL of the acid mixture with 150 mg of CNT_{syn} were maintained at 150 °C for 2 h. Following the functionalization, the CNT were washed with Milli-Q water several times until the pH value was close to 7 [31].

Synthesis of Ni/CNT template

Nickel NP were deposited on the CNT surface by direct chemical reduction of the nickel and ethylenediamine complex or $[\text{Ni}(\text{en})_2]^{2+}$. CNT were dispersed in CH_3OH and put at 80°C with constant stirring, then the $\text{NiCl}_2 \cdot 6\text{H}_2\text{O}$ was added and left to dissolve for 10 min and subsequently, the corresponding (en) was added to form the $[\text{Ni}(\text{en})_2]^{2+}$ complex, and left to react for 10 min. After complex formation in the presence of CNT, NaBH_4 methanolic solution was added gradually. Afterward, the reaction mixture was maintained for 2 h at 80°C. Finally, the product was filtered off and washed with methanol, Milli-Q water, and left to dry in an oven.

Synthesis of Pt-Ni/CNT by in situ galvanic displacement method at room temperature

For the in situ galvanic displacement reaction, the Ni/CNT material (5 mg) was dispersed in 10 mL of H₂O by ultrasound and immediately reacted with a 0.25 mmol L⁻¹ of Pt⁴⁺ ions from an aqueous solution of K₂PtCl₆. After 2 h, the reaction solution was filtered off and washed with H₂O and dried in an oven to obtain the Pt-Ni/CNT electrocatalyst.

Physical characterization of material

The study of the materials morphology was carried out by Field Emission Scanning Electron Microscopy (FE-SEM) with a JEOL JSM-7800F Schottky instrument. The samples were dispersed in methanol, and a drop was put over in a copper-carbon grid. The metallic contents and thermal stability were carried out by thermogravimetric analysis (TGA); these were performed on a TA-instrument Q50 TGA thermal analyzer. The TGA operating conditions employed were a heating rate of 20 °C min⁻¹, from room temperature to 850 °C with airflow at 60 mL min⁻¹. They were further confirming the exact metallic content by Inductively Coupled Plasma Optic Emission Spectroscopy (ICP-OES) Perkin Elmer Optima 8300 at 1300 Watts of radio frequency power. The operating conditions of ICP-OES were the plasma flow rate was at 15 L min⁻¹, the nebulizer gas flow was 1.5 L min⁻¹, auxiliary gas flow rate 0.2 L min⁻¹, and nebulization gas flow rate of 0.55 L min⁻¹. The wavelength for Pt and Ni were 265.94 and 352.45 nm, respectively.

Electrochemical characterization of materials

The electrochemical measurements were conducted using a potentiostat/galvanostat Biologic VMP-300 at room temperature with a three-electrode system with an Au spiral wire, Ag/AgCl/KCl(saturated) were used as counter electrodes, and reference, respectively; the working electrode employed was a glassy carbon rotating electrode (RDE) modified with the synthesized materials. The RDE modification was depositing 0.1142 mg cm⁻² from 40 μL of the synthesized electrocatalysts dispersed in Nafion® 117/ethanol (1/4:3/4 v/v) let dry at 25 °C. The surface electrochemical properties were investigated by cyclic voltammetry (CV) and were performed in N₂-saturated 0.5 mol L⁻¹ H₂SO₄ in the potential range of 0 to 1.2 V vs. reversible hydrogen electrode (RHE) at a scan rate of 100 mV s⁻¹. Subsequently, the CO-stripping test was recorded after the electrolyte solution was saturated with CO, and potential at 0.05 V for 180 s was applied. Afterward, the solution was bubbled with N₂ under the same conditions for 10 min.

Hydrogen fuel test

Since Pt-Ni/CNT was tested as a cathodic catalyst in the ORR, only the cathode gas diffuser was modified with Pt-Ni/CNT electrocatalyst. Commercial Pt/C was used as an anodic catalyst. The catalytic performance of synthesized Pt-Ni/CNT and commercial Pt/C catalyst was compared with normalized Pt loading at 0.5 mg cm⁻². The spraying process was employed to prepare the Membrane Electrode Assembly (MEA) with a surface area of 9 cm². Two modified gas diffusers were placed in a sandwich arrangement with a commercial Nafion 117 membrane separator. The MEA was pressed at 0.4-0.8 ton cm⁻² at 120 °C for 2 min. Afterward MEA fabrication, Nickel dissolution was carried out to decrease the metal loading; the leaching process was carried in a typical three-electrode cell with 0.5 mol L⁻¹ H₂SO₄ in the potential range of 0.3 to 1.1 V vs. reversible hydrogen electrode (RHE) and a scan rate of 100 mV s⁻¹ at different potential cycles (0, 170 and 1,000). CV, polarization curves, and electrochemical impedance spectroscopy (EIS) were performed using the potentiostat/galvanostat Solartron model 1287 with 20 A booster and Solartron model 1290 with Impedance/Gain analyzer model 1260, respectively.

Results and discussion

Physicochemical characterization of materials

The metallic content and thermal stability of the synthesized materials were determined by TGA (Fig. 1). The CNT_{syn} sample is thermally stable up to 460 °C, in comparison to CNT that shows a reaction around 350 °C with a decomposition of 1.5 wt%, and the decomposition is associated with the thermal oxidation of

carbonyl groups (C=O, C-OH, and C-OOH) formed during the acid treatment as diverse authors report [32]. For Pt-Ni/CNT sample, the thermal stability and metal composition are shown in Table 1. Pt-Ni/CNT showed lower thermal stability compared with Ni/CNT and CNT samples. This change can be attributed to O molecules adsorption over Pt-Ni/CNT, and this transfer to carbon support, promoting the accelerated oxidation of CNT structure and transforming it to CO₂ [33]. Furthermore, final residual weights at 700°C of Ni/CNT and Pt-Ni/CNT were 5.94 and 8.17%, respectively. Also, from the thermograms in Fig. 1, the metallic contents of Pt-Ni/CNT sample were determined, and this was of 2.23 wt% and was corroborated by ICP-OES measurement; while the concentration of Pt was of 2.23 wt%, and Ni was of 1.98 wt%.

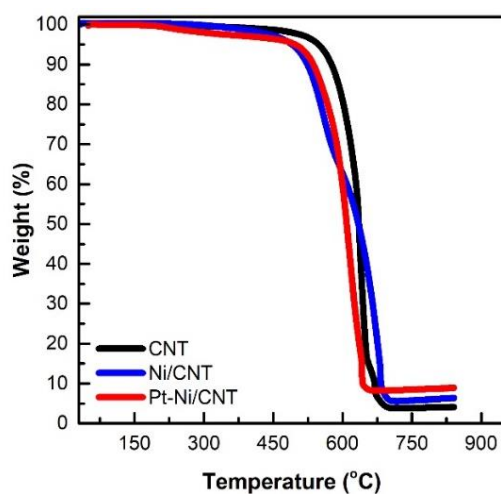


Fig. 1. Thermograms of CNT, Ni/CNT, and Pt-Ni/CNT materials.

Table 1. Summary of metallic loading obtained by TGA for Pt-Ni/CNT in each stage of the synthesis.

	Metal residue	Relation % weight		
		M _x O _y	Fe %	Ni %
CNT _{syn}	7.49	2.62	-	-
CNT	3.85	1.35	-	-
Ni/CNT	5.94	1.32	1.98	-
Pt-Ni/CNT	8.17	1.30	1.95	2.23

Once the Pt and Ni presence was identified, the particles' morphology was analyzed by microscopy, as shown in Fig. 2. The micrograph of Ni particles deposited on the CNT is shown in Fig. 2a); in the micrographs, CNT's characteristic tubular structure and small metal particles are deposited on CNT. However, the distribution of Ni particles on CNT was not evident in the micrographs. Therefore, the elemental mapping analysis was performed, as shown in Fig. 2b). Based on map analysis, the uniform scattered distribution of Ni particles can be appreciated

The Pt-Ni/CNT samples micrograph shown in Figure 3a; reveals the Ni and Pt metals deposited on carbon nanotubes. Fig. 3b) shows the elemental mapping, which confirms Pt and Ni metals evenly distributed throughout the CNT surface. The bimetallic particles are homogeneously distributed on CNT, as shown in Figures 3c) and 3d), respectively.

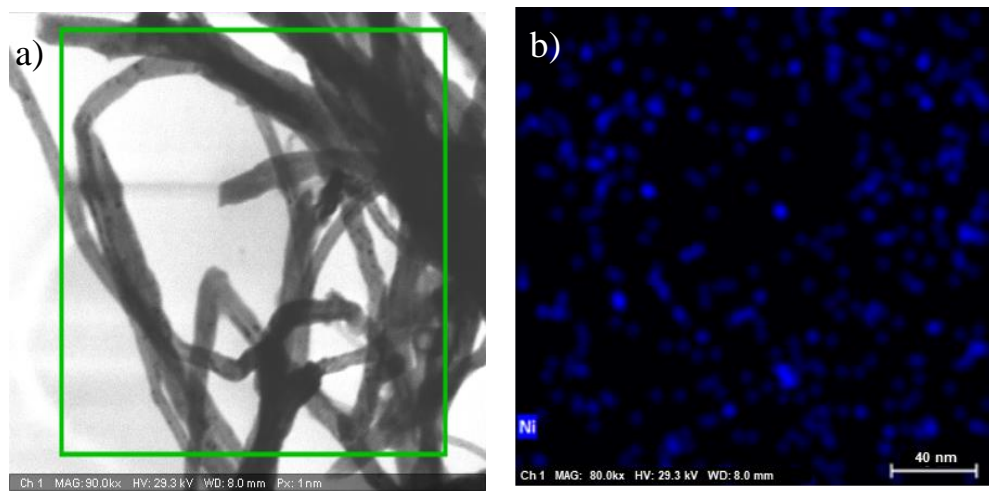


Fig. 2. Ni/CNT template **a)** FE-SEM image and **b)** Ni EDS mapping.

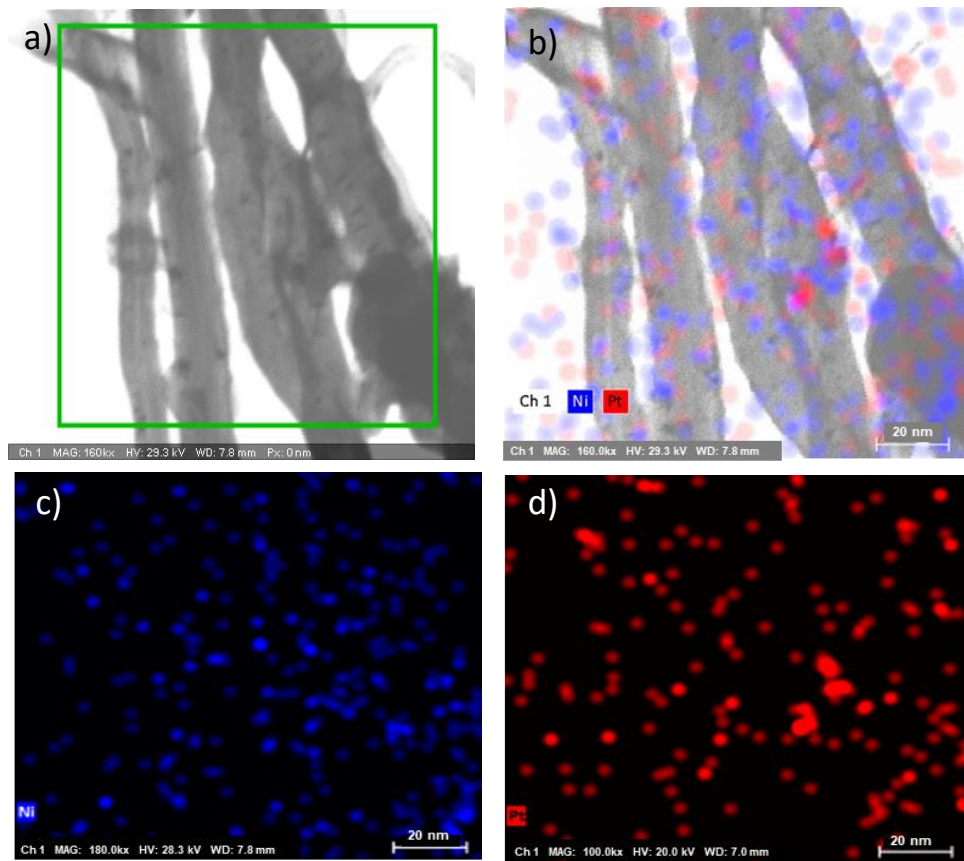


Fig. 3. Pt-Ni/CNT electrocatalyst **a)** FE-SEM image, **b)** EDS mapping of Ni and Pt, **c)** elemental mapping of Ni, and **d)** elemental mapping of Pt.

Electrocatalyst performance of Pt-Ni/CNT sample in the PEMFC

Fig. 4 shows Ni electrochemical dealloying in Pt-Ni/CNT sample to prepare the cathodic catalyst for the PEMFC test, applying different potential cycles (0, 170, and 1000 cycles). The Pt-Ni/CNT samples cyclic voltammograms show variations in the current of hydrogen adsorption/desorption zone for Pt surface between -0.2 to 0.6 V vs. RHE. In the anodic peak corresponding to hydrogen desorption from Pt surface, can be observed the current increases with the number of potential cycles, so this effect can be explained by the Pt-Ni/CNT catalyst surface restructuring, due to Ni atoms dealloying by the H_2SO_4 electrolyte during the potential cycling process, as reported in the literature previously [34].

The hydrogen desorption charge consumption (Q_H) by Pt-Ni/CNT catalyst at the different potential cycles is summarized in Table 2. The Q_H increases with increasing potential cycle number, confirming Ni atoms dealloying and forming a Pt-layer on the Pt-Ni/CNT catalyst surface as previously reported by Glüsen et al. Pt can explain this behavior as the active phase for hydrogen adsorption/desorption process. The ECSA also evaluated in the hydrogen zone followed the same trend to respect potential cycles [35,36].

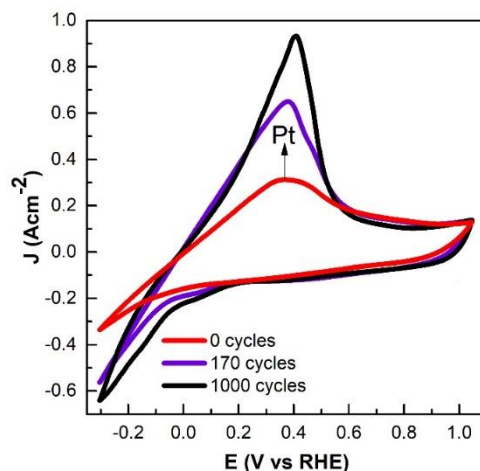


Fig. 4. Cyclic voltammogram of Pt-Ni/CNT electrocatalyst dealloying.

After Nickel atoms were dealloyed from Pt-Ni/CNT catalyst surface by different potential cycles, the fuel cell's catalytic performance was evaluated. Fig. 5 shows the polarization curve at 60 °C using Pt-Ni/CNT electrocatalyst at different potential cycles to increase Pt-layer surface and can be observed the typically open circuit and activation losses.

The Pt-Ni/CNT at 0 potential cycles show the lowest loss in polarization voltage in accordance with Q_H and ECSA values reported in Table 2. The results of Pt-Ni/CNT electrocatalyst at 0 potential cycles indicate that the electrocatalyst surface show a low concentration of Pt, compared with the Pt-Ni/CNT at 1000 potential cycles. The Pt-Ni/CNT at 1000 potential cycles shows the maximum power density of 220 mW cm^{-2} , confirming the Pt-layers were increasing over the Pt-Ni/CNT electrocatalyst surface by the electrochemical restructuration by potential cycles. Some authors report that the dealloying and leaching of less noble metal of bimetallic electrocatalyst can generate a porous structure by the migration of Ni atoms to the particle inside when the synthesis method generates core-shell particles by the galvanic displacement method [23,34,37,38]. Therefore, the fuel cell improvement in power density with Pt-Ni/CNT cathodic catalyst is attributed to Ni atoms dealloying to the H_2SO_4 electrolyte solution; and the enrichment of the electrocatalyst surface with a Pt-layer [39].

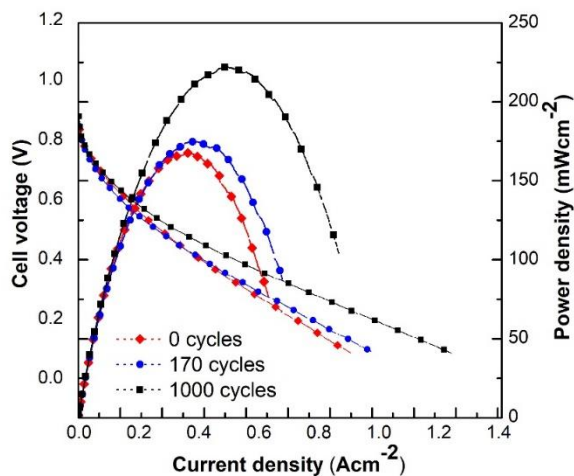


Fig. 5. Polarization curves of cathodic Pt-Ni/CNT electrocatalyst at different potential cycles.

Table 2. Electrochemical data of the Pt-Ni/CNT electrocatalyst with different activation cycles.

cycles	Q _H (mC)	*ECSA _H (m ² g ⁻¹)	P _{max} (mWcm ⁻²)
0	10.80	6.04	167
170	136.89	76.61	199
1000	199.76	111.80	220

*ECSA_H was determined in the MEA

The Pt-Ni/CNT electrocatalysts catalytic performance was compared with Pt/C electrocatalyst at 1000 potential cycles both, as shown in Fig. 6. The polarization curve shows that Pt/C electrocatalyst produces the maximum power density of 350 mW cm⁻² 20wt% metallic content of pure platinum.

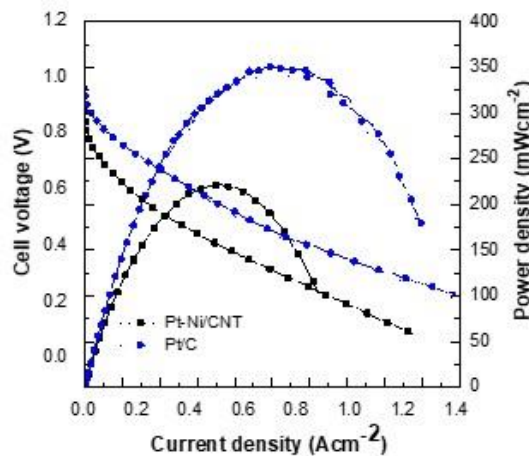


Fig. 6. Comparison of the polarization curves of Pt-Ni/CNT and commercial Pt/C at 1000 potential cycles.

The results indicate that the Pt-Ni/CNT electrocatalyst produces a 63% power density of the commercial Pt/C electrocatalyst with 90wt% fewer metal contents than reports in the literature. Lin et al. reported the catalytic performance of $\text{Pt}_1\text{Ni}_1/\text{C}$ electrocatalyst with 30%wt metallic content, with a power density of 369.7 mW cm^{-2} , very similar to a Pt/C commercial electrocatalyst. However, an evident decline in the catalytic activity after 1000 cycles was observed to 288 mW cm^{-2} [40]. Literature results indicate that high metallic contents poison the MEA of the PEMFC, reducing the catalytic performance because the dealloyed metal can be deposited in the MEA surface, blocking fuel diffusion. In Table 3 the power density generated before and after potential cycles of Pt-Ni electrocatalyst in the PEMFC are compared, normalized with respect to the Pt amount are reported.

Table 3. Summary of the reported normalized power density with the amount of Pt.

Materials	$P_{\max} (\text{mWmgPt}^{-1}\text{cm}^{-2})$	Reference
Pt-Ni/CNT 0 cycles	2385.71	this work
Pt-Ni/CNT 170 cycles	2842.85	this work
Pt-Ni/CNT 1000 cycles	7142.86	this work
$\text{Pt}_1\text{Ni}_1/\text{C}$ 0 cycles	1051.14	25
$\text{Pt}_1\text{Ni}_1/\text{C}$ 1000 cycles	800	25
PtNi/GNPs	1350	7
PtNiCo/C	1000	26
$\text{Pt}_3\text{Ni}_1/\text{NCB}$	3280	6

The ultra-low concentration of Pt and Ni metals in the Pt-Ni/CNT electrocatalyst does not affect the MEA performance with potential cycles than Lin et al. reported, as shown in Table 3. The synthesized Pt-Ni/CNT electrocatalyst with ultra-low Pt and Ni contents generated 8.93 times more power density at 1000 potential cycles compared to similar electrocatalysts with high metallic contents

Electrochemical characterization

The most popular methods to assess the ECSA are the underpotential deposition of hydrogen (Hupd) and CO stripping voltammetry in a three-electrode system [41,42]. The study of Hupd and CO stripping at different potential cycles for Pt-Ni/CNT electrocatalyst are shown in Fig. 7. The black lines voltammograms show the Hupd region between 0 to 0.26 V vs. RHE as a sharp peak, attributed to the hydrogen adsorption/desorption process. The blue line voltammograms evaluate the surface properties of Pt-Ni/CNT electrocatalyst by the CO electrochemical oxidation. The region between 0.73 to 1.00 V vs. RHE shows the anodic peak, attributed to the adsorbed CO oxidation [43,44].

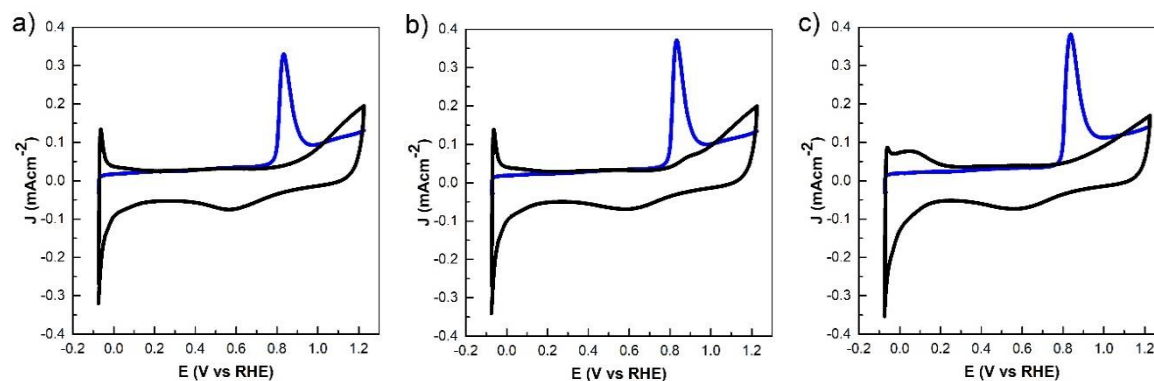


Fig. 7. Pt-Ni/CNT electrocatalyst CO stripping voltammogram at 0 (a), 170 (b), and 1000 (c) at 50 mV s^{-1} in $\text{H}_2\text{SO}_4 0.5 \text{ M}$. Black-line (CO absence) and blue-line (CO presence).

ECSA_H values were calculated from the hydrogen desorption charge in the potential region from 0 to 0.26 V vs. RHE using the equation (1), and ECSA_{CO} values were calculated from the charge associated with CO oxidation in the potential region from 0.73 to 1.00 V vs. RHE using the equation (2). Where Q_H is the charge in mC determined by integration of hydrogen desorption region, Q_{CO} is the charge in mC determined by integration of CO oxidation peak, 0.210 mC cm⁻² corresponds to hydrogen adsorption/desorption on polycrystalline Pt, 0.420 mC cm⁻² corresponds to a monolayer of CO adsorbed and L_{Pt} . The Pt loading on the surface determined by ICP-IOS and TGA is seen in table 1 [45]. Furthermore, the ratio between the ECSAs can be calculated, as shown in equation 3 [46].

$$ECSA_H = \frac{Q_H}{(0.210 \text{ mC cm}^{-2}) L_{Pt}} \quad (1)$$

$$ECSA_{CO} = \frac{Q_{CO}}{(0.420 \text{ mC cm}^{-2}) L_{Pt}} \quad (2)$$

$$ratio \text{ ECSAs} = \frac{ECSA_{CO}}{ECSA_H} \quad (3)$$

The ESCA results of Pt-Ni/CNT electrocatalyst at different potential cycles are shown in Table 4. The calculated ECSA_H and ECSA_{CO} and ECSA_H ratio, the Pt-Ni/CNT at 0, 170, and 1000 activation cycles were 3.58, 3.25, and 1.58, respectively, where values greater than 1.5 of ECSAs ratio suggest forming a Pt-skin-terminated of Pt(111) as surface structure [13,17,47].

Table 4. ECSAs of the Pt-Ni/CNT electrocatalyst at different activation cycles.

cycles	ECSA _{CO} (m ² g ⁻¹)	ECSA _H (m ² g ⁻¹)*
0	35.04	9.79
170	39.45	12.15
1000	47.08	29.86

*ECSA_H was determined in a three-electrode system in the half cell.

The electrochemical characterization shows the effect of potential cycles over ECSA of Pt-Ni/CNT determined by Hupd and CO stripping and corroborated MEA results in the PEMFC, where the electrochemical dealloying modified Pt-Ni/CNT electrochemical surface, increasing the Pt-layer exposure in catalyst surfaces, explaining the increase of the ECSA [34].

Conclusion

In this work, the Pt-Ni/CNT material was successfully synthesized for use as a cathodic electrocatalyst in PEM fuel cell technology. The performance of this electrocatalyst was improved with potential cycles. This, mainly due to the Pt surface restructuration by Ni atoms lixiviation. The Pt surface restructuration promotes that the ECSA increases with the number of potential cycles and suggests the optimization of Pt electrocatalysts sites; this is observed both in the cell in solution and in the fuel cell assembly. The maximum power density obtained for Pt-Ni/CNT with 1000 potential cycles was lower than shown by the commercial catalyst Pt/C, however, with an ultra-low amount of platinum present in the bimetallic catalyst (about 2%) compared to the

20% content of Pt in the commercial catalyst. However, with a better power generation per gram of platinum, reducing the cost of energy generation.

Acknowledgements

The authors thank Tijuana Technological Institute for providing the facilities for this research. D. M. Lopez-Rosas wishes to thank CONACyT for the doctoral scholarship. The authors also thank CONACyT-SENER and TecNM for financial assistance through the projects 292862 and 8080.20-P, respectively.

References

1. Meyer, Q.; Zeng, Y.; Zhao, C. *Adv. Mater.* **2019**, *31* (40), 1901900 DOI: <https://doi.org/10.1002/adma.201901900>
2. Wang, L.; Wan, X.; Liu, S.; Xu, L. Shui, J. J. *Energy Chem.* **2019**, *39*, 77-87 DOI: <https://doi.org/10.1016/j.jecchem.2018.12.019>
3. Singh, K.; Tetteh, E. B.; Lee, H.-Y.; Kang, T.-H.; Yu, J.-S. *ACS Catal.* **2019**, *9* (9), 8622-8645 DOI: <https://doi.org/10.1021/acscatal.9b01420>
4. Safo, I. A.; Dosche, C.; Özaslan, M. *Chemphyschem.* **2019**, *20* (22), 3010-3023 DOI: <https://doi.org/10.1002/cphc.201900653>
5. Beermann, V.; Holtz, M. E.; Padgett, E.; de Araujo, J. F.; Muller, D. A.; Strasser, P. *Energy Environ. Sci.* **2019**, *12* (8), 2476-2485 DOI: <https://doi.org/10.1039/C9EE01185D>
6. Yang, H.; Ko, Y.; Lee, W.; Züttel, A.; Kim, W. *Mater. Today Energy* **2019**, *13*, 374-381 DOI: <https://doi.org/10.1016/j.mtener.2019.06.007>
7. Daş, E.; Alkan Gürsel, S.; Bayrakçeken Yurtcan, A. J. *Supercrit. Fluids* **2020**, *165*, 104962 DOI: <https://doi.org/10.1016/j.supflu.2020.104962>
8. Sudirman, S.; Adi, W.; Budianto, E.; Khaerudini, D.; Yudianti, R. *Int. J. of Chem.* **2019**, *12*, 37 DOI: <https://doi.org/10.5539/ijc.v12n1p37>
9. Liu, Z.; Abdelhafiz, A. A.; Jiang, Y.; Qu, C.; Chang, I.; Zeng, J.; Liao, S.; Alamgir, F. M. *Mater. Chem. Phys.* **2019**, *225*, 371-378 DOI: <https://doi.org/10.1016/j.matchemphys.2018.12.100>
10. Daş, E.; Kaplan, B. Y.; Gürsel, S. A.; Yurtcan, A. B. *Renew. Energy* **2019**, *139*, 1099-1110 DOI: <https://doi.org/10.1016/j.renene.2019.02.137>
11. Guzman, C.; Verde, Y.; Bustos, E.; Manriquez, F.; Terol, I.; Arriaga, L. G.; Orozco, G. *ECS Trans.* **2019**, *20* (1), 413-423 DOI: <https://doi.org/10.1149/1.3268409>
12. Bharti, A.; Cheruvally, G. J. *Power Sources* **2017**, *360*, 196-205 DOI: <https://doi.org/10.1016/j.ipowrsour.2017.05.117>
13. Chen, C.; Kang, Y.; Huo, Z.; Zhu, Z.; Huang, W.; Xin, H. L.; Snyder, J. D.; Li, D.; Herron, J. A.; Mavrikakis, M.; Chi, M.; More, K. L.; Li, Y.; Markovic, N. M.; Somorjai, G. A.; Yang, P.; Stamenkovic, V. R. *Sci.* **2014**, *343* (6177), 1339-1343 DOI: <https://doi.org/10.1126/science.1249061>
14. Wang, Z.; Yao, X.; Kang, Y.; Miao, L.; Xia, D.; Gan, L. *Adv. Funct. Mater.* **2019**, *29* (35), 1902987 DOI: <https://doi.org/10.1002/adfm.201902987>
15. Singh, K.; Tetteh, E. B.; Lee, H.-Y.; Kang, T.-H.; Yu, J.-S. *ACS Catal.* **2019**, *9* (9), 8622-8645 DOI: <https://doi.org/10.1021/acscatal.9b01420>
16. Gan, L.; Heggen, M.; Rudi, S.; Strasser, P. *Nano Lett.* **2012**, *12* (10), 5423-5430 DOI: <https://doi.org/10.1021/nl302995z>
17. Becknell, N.; Kang, Y.; Chen, C.; Resasco, J.; Kornienko, N.; Guo, J.; Markovic, N. M.; Somorjai, G. A.; Stamenkovic, V. R.; Yang, P. *J. Am. Chem. Soc.* **2015**, *137* (50), 15817-15824 DOI: <https://doi.org/10.1021/jacs.5b09639>
18. Ghosh Chaudhuri, R.; Paria, S. *Chem. Rev.* **2012**, *112* (4), 2373-2433 DOI: <https://doi.org/10.1021/cr100449n>

19. Alia, S. M.; Yan, Y. S.; Pivoval, B. S. *Catal. Sci. Technol.* **2014**, 4 (10), 3589-3600 DOI: <https://doi.org/10.1039/C4CY00736K>

20. Ercolano, G.; Farina, F.; Stievano, L.; Jones, D. J.; Rozière, J.; Cavaliere, S. *Catal. Sci. Technol.* **2019**, 9 (24), 6920-6928 DOI: <https://doi.org/10.1039/C9CY01514K>

21. Kang, Y. S.; Jung, J. Y.; Choi, D.; Sohn, Y.; Lee, S.-H.; Lee, K.-S.; Kim, N. D.; Kim, P.; Yoo, S. J. *ACS Appl. Mater. Interfaces* **2020**, 12 (14), 16286-16297 DOI: <https://doi.org/10.1021/acsmami.9b22615>

22. Oezaslan, M.; Hasché, F.; Strasser, P. *J. Phys. Chem. Lett.* **2013**, 4 (19), 3273-3291 DOI: <https://doi.org/10.1021/jz4014135>

23. Tian, X.; Zhao, X.; Su, Y.-Q.; Wang, L.; Wang, H.; Dang, D.; Chi, B.; Liu, H.; Hensen, E. J. M.; Lou, X. W.; Xia, B. Y. *Science* **2019**, 366 (6467), 850-856 DOI: <https://doi.org/10.1126/science.aaw7493>

24. Pavlišić, A.; Jovanović, P.; Šelih, V. S.; Šala, M.; Bele, M.; Dražić, G.; Arčon, I.; Hočvar, S.; Kokalj, A.; Hodnik, N.; Gaberšček, M. *ACS Catal.* **2016**, 6 (8), 5530-5534 DOI: <https://doi.org/10.1021/acscatal.6b00557>

25. Ho, F. F. L.; Reilley, C. N. *Anal. Chem.* **1969**, 41 (13), 1835-1841 DOI: <https://doi.org/10.1021/ac60282a008>

26. De Stefano, C.; Foti, C.; Sammartano, S. *J. Chem. Eng. Data* **1999**, 44 (4), 744-749 DOI: <https://doi.org/10.1021/je980319n>

27. Yang, Y.; Li, S.; Xie, C.; Liu, H.; Wang, Y.; Mei, Q.; Liu, H.; Han, B. *Chin. Chem. Lett.* **2019**, 30 (1), 203-206 DOI: <https://doi.org/10.1016/j.cclet.2018.04.006>

28. Zhang, L.; Chu, X.; Yuan, S.-m.; Zhao, G.-c. *RSC Adv.* **2015**, 5 (52), 41317-41323 DOI: <https://doi.org/10.1039/C5RA03306C>

29. Watkins, C. L.; Vigée, G. S. *J. Phys. Chem. A* **1976**, 80 (1), 83-88 DOI: <https://doi.org/10.1021/j100542a018>

30. Tsierkezos, N.; Schröder, D.; Schwarz, H. *Int. J. Mass Spectrom.* **2004**, 235, 33-42 DOI: <https://doi.org/10.1016/j.ijms.2004.03.005>

31. Reyes-Cruzaley, A. P.; Félix-Navarro, R. M.; Trujillo-Navarrete, B.; Silva-Carrillo, C.; Zapata-Fernández, J. R.; Romo-Herrera, J. M.; Contreras, O. E.; Reynoso-Soto, E. A. *Electrochim. Acta* **2019**, 296, 575-581 DOI: <https://doi.org/10.1016/j.electacta.2018.11.023>

32. Osorio, A. G.; Silveira, I. C. L.; Bueno, V. L.; Bergmann, C. P. *Appl. Surf. Sci.* **2008**, 255 (5, Part 1), 2485-2489 DOI: <https://doi.org/10.1016/j.apsusc.2008.07.144>

33. Rodriguez, J. R.; Félix, R. M.; Reynoso, E. A.; Gochi-Ponce, Y.; Gómez, Y. V.; Moyado, S. F.; Alonso-Núñez, G. J. *Energy Chem.* **2014**, 23 (4), 483-490 DOI: [https://doi.org/10.1016/S2095-4956\(14\)60175-3](https://doi.org/10.1016/S2095-4956(14)60175-3)

34. Baldizzone, C.; Gan, L.; Hodnik, N.; Keeley, G. P.; Kostka, A.; Heggen, M.; Strasser, P.; Mayrhofer, K. J. J. *ACS Catal.* **2015**, 5 (9), 5000-5007 DOI: <https://doi.org/10.1021/acscatal.5b01151>

35. Glüsen, A.; Dionigi, F.; Paciok, P.; Heggen, M.; Müller, M.; Gan, L.; Strasser, P.; Dunin-Borkowski, R. E.; Stolten, D. *ACS Catal.* **2019**, 9 (5), 3764-3772 DOI: <https://doi.org/10.1021/acscatal.8b04883>

36. Erlebacher, J. *Phys. Rev. Lett.* **2011**, 106 (22), 225504 DOI: <https://doi.org/10.1103/PhysRevLett.106.225504>

37. Wang, D.; Zhao, P.; Li, Y. *Sci. rep.* **2011**, 1, 37 DOI: <https://doi.org/10.1038/srep00037>

38. Rudi, S.; Gan, L.; Cui, C.; Gliech, M.; Strasser, P. *J. Electrochem. Soc.* **2015**, 162 (4), F403-F409 DOI: <https://doi.org/10.1149/2.0621504jes>

39. Tuaev, X.; Rudi, S.; Petkov, V.; Hoell, A.; Strasser, P. *ACS Nano* **2013**, 7 (7), 5666-5674 DOI: <https://doi.org/10.1021/nn402406k>

40. Lin, R.; Che, L.; Shen, D.; Cai, X. *Electrochim. Acta* **2020**, 330, 135251 DOI: <https://doi.org/10.1016/j.electacta.2019.135251>

41. Rudi, S.; Cui, C.-H.; Gan, L.; Strasser, P. *Electrocatalysis* **2014**, 5, 408-418 DOI: <https://doi.org/10.1007/s12678-014-0205-2>

42. Urchaga, P.; Baranton, S.; Coutanceau, C. *Electrochim. Acta* **2013**, 92, 438-445 DOI: <https://doi.org/10.1016/j.electacta.2013.01.042>

43. Takeshita, T.; Kamitaka, Y.; Shinozaki, K.; Kodama, K.; Morimoto, Y. *J. Electroanal. Chem.* **2020**, 871, 114250 DOI: <https://doi.org/10.1016/j.jelechem.2020.114250>
44. Rudi, S.; Teschner, D.; Beermann, V.; Hetaba, W.; Gan, L.; Cui, C.; Gliech, M.; Schlögl, R.; Strasser, P. *ACS Catal.* **2017**, 7 (9), 6376-6384 DOI: <https://doi.org/10.1021/acscatal.7b00996>
45. Vidaković, T.; Christov, M.; Sundmacher, K. *Electrochim. Acta* **2007**, 52 (18), 5606-5613 DOI: <https://doi.org/10.1016/j.electacta.2006.12.057>
46. Becknell, N.; Son, Y.; Kim, D.; Li, D.; Yu, Y.; Niu, Z.; Lei, T.; Snead, B. T.; More, K. L.; Markovic, N. M.; Stamenkovic, V. R.; Yang, P. *J. Am. Chem. Soc.* **2017**, 139 (34), 11678-11681 DOI: <https://doi.org/10.1021/jacs.7b05584>
47. van der Vliet, D. F.; Wang, C.; Li, D.; Paulikas, A. P.; Greeley, J.; Rankin, R. B.; Strmcnik, D.; Tripkovic, D.; Markovic, N. M.; Stamenkovic, V. R. *Angew. Chem. Int. Ed.* **2012**, 51 (13), 3139-3142 DOI: <https://doi.org/10.1002/anie.201107668>